

KMT-2025-BLG-1314 and KMT-2025-BLG-1392: two microlensing planetary/brown-dwarf candidates analyzed with differentiable code

Haibin Ren¹, Weicheng Zang², Wei Zhu¹, Yoon-Hyun Ryu³, Yuchen Tang², Jiyuan Zhang¹, Michael D. Albrow⁴, Sun-Ju Chung³, Andrew Gould^{5,6}, Cheongho Han⁷, Kyu-Ha Hwang³, Youn Kil Jung^{3,8}, In-Gu Shin², Yossi Shvartzvald⁹, Hongjing Yang^{10,2}, Jennifer C. Yee¹¹, Dong-Jin Kim³, Chung-Uk Lee³, Byeong-Gon Park³, Yunyi Tang¹, Dan Maoz¹², Shude Mao², Qiyue Qian^{2,1}

¹ Department of Astronomy, Tsinghua University, Beijing 100084, China;

² Department of Astronomy, Westlake University, Hangzhou 310030, Zhejiang Province, China

³ Korea Astronomy and Space Science Institute, Daejeon 34055, Republic of Korea

⁴ University of Canterbury, School of Physical and Chemical Sciences, Private Bag 4800, Christchurch 8020, New Zealand

⁵ Max-Planck-Institute for Astronomy, Königstuhl 17, 69117 Heidelberg, Germany

⁶ Department of Astronomy, Ohio State University, 140 W. 18th Ave., Columbus, OH 43210, USA

⁷ Department of Physics, Chungbuk National University, Cheongju 28644, Republic of Korea

⁸ National University of Science and Technology (UST), Daejeon 34113, Republic of Korea

⁹ Department of Particle Physics and Astrophysics, Weizmann Institute of Science, Rehovot 7610001, Israel

¹⁰ Westlake Institute for Advanced Study, Hangzhou 310030, Zhejiang Province, China

¹¹ Center for Astrophysics | Harvard & Smithsonian, 60 Garden St., Cambridge, MA 02138, USA

¹² School of Physics and Astronomy, Tel-Aviv University, Tel-Aviv 6997801, Israel

Received 20XX Month Day; accepted 20XX Month Day

Abstract Analysis of binary-lens microlensing events typically requires intensive computation because of the multimodal and complex posterior distributions. With the recent development of the JAX-based differentiable binary-lensing modeling package `microlux`, we present an analysis of two microlensing events with planet/brown-dwarf candidates, KMT-2025-BLG-1314 and KMT-2025-BLG-1392. Both events exhibit the “Close/Wide” degeneracy, and KMT-2025-BLG-1314 suffers from the “Planet/Binary” degeneracy and a recently recognized “Point/Finite” degeneracy among the planetary solutions. For KMT-2025-BLG-1314, the binary mass ratio is $\log q \sim -3.5$ for the planetary solutions and $\log q > -1.5$ for the binary solutions, while for KMT-2025-BLG-1392 we find $\log q \sim -1.3$. We show that for the analysis of KMT-2025-BLG-1314, Hamiltonian Monte Carlo (HMC), enabled by

`microlux`, provides robust parameter inference and outperforms traditional Markov chain Monte Carlo (MCMC) methods in the presence of bimodal posteriors.

Key words: gravitational lensing; micro - planets and satellites; detection - methods: statistical

1 INTRODUCTION

Gravitational microlensing has been widely applied to a broad range of astrophysical problems, most notably the detection of exoplanets and stellar binaries (Mao & Paczynski 1991; Gould & Loeb 1992). As of 2026 January ¹, more than 263 exoplanets have been discovered via microlensing, according to the NASA Exoplanet Archive (Christiansen et al. 2025). This growing planet sample enables statistical studies of exoplanet demographics (Zhu & Dong 2021), especially the cold planet population (e.g., Shvartzvald et al. 2016; Zang et al. 2025).

Almost all of the microlensing planets are discovered by ground-based surveys toward the Galactic bulge. These include the Optical Gravitational Lensing Experiment (OGLE, Udalski et al. 2015), the Microlensing Observations in Astrophysics survey (MOA, Sako et al. 2008), and the Korea Microlensing Telescope Network (KMTNet, Kim et al. 2016). Upcoming space-based missions, including the Nancy Grace Roman Space Telescope (Penny et al. 2019), the Earth 2.0 Microlensing Telescope (Gould et al. 2021; Ge et al. 2022), and the Chinese Space Station Telescope (CSST, Yan & Zhu 2022), are expected to increase the number of microlensing planetary detections to the thousands and systematically discover currently rare systems/objects, including dark lenses (Sahu et al. 2022; Lam et al. 2022; Mróz et al. 2022), free-floating planets (Mróz et al. 2017; Gould et al. 2022; Sumi et al. 2023), and lenses with multiple components (e.g., Gaudi et al. 2008).

Along with the success in the discovery front, the detailed analysis of binary-lens and multiple-lens microlensing events remains a challenge. The inherently complex parameter space is characterized by strong correlation/continuous degeneracy (e.g., Gaudi & Gould 1997), multi-modality (e.g., the well-known close-wide degeneracy, Griest & Safizadeh 1998; Dominik 1999; An 2005), and high-order effects (e.g., the microlensing parallax and xallarap effects, Gould 1992; Griest & Hu 1992). Typical modeling approaches combine brute-force searches, template matching (Liebig et al. 2015; Bozza 2024), and other global optimization techniques to explore the multi-modal parameter space, followed by Markov chain Monte Carlo (MCMC) sampling to characterize the local posterior distributions and estimate parameter uncertainties. However, conventional MCMC methods often struggle with posterior distributions that exhibit strong non-linear correlations, high dimensionality, and multiple modes, leading to inefficient sampling, strong auto-correlations, and poor convergence across different chains, ultimately degrading the accuracy of the inferred parameters.

The development of the automatic differentiation technique has made it possible to obtain accurate gradients even for complicated models. This then promotes the use of gradient-based sampling techniques like Hamiltonian Monte Carlo (HMC; Duane et al. 1987; Neal 2011; Hoffman & Gelman 2011) in many modern

¹ Based on a query made in January 2026

probabilistic programming languages, such as `Stan` (Carpenter et al. 2017), `Numpyro` (Phan et al. 2019), and `Blackjax` (Cabezas et al. 2024)). An emerging trend in astronomy is to develop differentiable code based on automatic differentiation packages (e.g., `Julia` Bezanson et al. 2017 and `Jax` Bradbury et al. 2018), and successful applications are seen across a wide range of research fields (an incomplete list can be found here ^{2 3}). In microlensing, several differentiable models have been developed, including `caustics` (Bartolić 2023), `microlux` (Ren & Zhu 2025), and `microJAX` (Miyazaki & Kawahara 2025). Among these, `microlux` is unique for its specially designed error estimator with adaptive contour integration (Bozza 2010; Bozza et al. 2018; Bozza et al. 2025). This can ensure the convergence of both the microlensing magnification and its derivatives. So far, applications of these differentiable models are limited to either synthetic data or well-studied historical events.

Here we present the analysis of two microlensing binary-lens events, KMT-2025-BLG-1314 and KMT-2025-BLG-1392, based on the differentiable model of `microlux`. Both events were discovered by KMTNet and followed up by the Microlensing Astronomy Probe (MAP) program using the Las Cumbres Observatory Global Telescope (LCOGT; Brown et al. 2013) network. The MAP program targets high-magnification microlensing events and has observed about a dozen planets to date, including two systems that each contains two planet-like companions (Zang et al. 2021; Li et al. 2026).

This paper is organized as follows: Section 2 describes the survey and follow-up observations, Section 3 presents the binary-lens single-source (2L1S) and single-lens binary-source (1L2S) modeling, Section 4 shows the source and lens properties with the color-magnitude diagram (CMD) and Bayesian analysis, respectively. Finally, in Section 5, we discuss the lessons learned from the differentiable modeling, focusing especially on the HMC method.

2 OBSERVATIONS

The microlensing events KMT-2025-BLG-1314 and KMT-2025-BLG-1392 were first alerted by the KMTNet AlertFinder system (Kim et al. 2018b) on 2025 June 10 and June 17, respectively. The observations were obtained with 1.6 m telescopes equipped with 4 deg² mosaic CCD cameras at Cerro Tololo Inter-American Observatory (CTIO) in Chile (KMTC), the South African Astronomical Observatory (SAAO) in South Africa (KMTS), and Siding Spring Observatory (SSO) in Australia (KMTA). Most KMTNet images were taken in the *I* band, with $\sim 9\%$ obtained in the *V* band to measure the source color.

The source star of KMT-2025-BLG-1314 is located at equatorial coordinates $(\alpha, \delta) = (17:30:12.47, -30:31:14.81)$, corresponding to Galactic coordinates $(\ell, b) = (-3.1299^\circ, +1.9777^\circ)$. This event lies in the KMTNet BLG11 field, which is monitored with an observing cadence of 0.4 hr⁻¹ for KMTC and 0.3 hr⁻¹ for KMTA and KMTS. The source star of KMT-2025-BLG-1392 is located at equatorial coordinates $(\alpha, \delta) = (17:43:28.63, -26:29:26.41)$, corresponding to Galactic coordinates $(\ell, b) = (+1.8371^\circ, +1.6827^\circ)$. This event lies in the KMTNet BLG18 field, with an observing cadence of 1.0 hr⁻¹ for KMTC and 0.8 hr⁻¹ for KMTA and KMTS. The KMTNet field layout is shown in Figure 12 of Kim et al. (2018a).

² <https://juliaastro.org/home/>

³ <https://github.com/JAXtronomy/awesome-JAXtronomy>

Following alerts issued by the KMTNet HighMagFinder system (Yang et al. 2022), follow-up observations were conducted by LCOGT and KMTNet. HighMagFinder is designed to identify high-magnification KMTNet events using real-time photometry before they reach a magnification threshold of $A_{\text{thresh}} = 25$, enabling timely follow-up observations. For KMT-2025-BLG-1314, LCOGT observations were carried out using the 1 m telescopes at SSO and SAAO, which we designate LCOA and LCOS, respectively. For KMT-2025-BLG-1392, MAP used the two 1 m telescopes at LCOGT-SSO (LCOA01 and LCOA02) and the 1 m telescope at the LCOGT Teide Observatory in Tenerife, Spain (LCOT), to monitor the event during its peak. All LCOGT observations were obtained in the I band. KMTNet employed its “auto-followup” mode to increase the observational cadence near the peak. For KMT-2025-BLG-1314, the KMTA cadence was raised from 0.3 hr^{-1} to $\Gamma = 3.3 \text{ hr}^{-1}$ through the substitution of BLG43 observations with those from BLG11. A similar strategy was applied to KMTS, for which replacing BLG03 with BLG11 observations resulted in the same increase in cadence, from 0.3 hr^{-1} to $\Gamma = 3.3 \text{ hr}^{-1}$. For KMT-2025-BLG-1392, the KMTA observing cadence increased from 0.8 hr^{-1} to $\Gamma = 3.8 \text{ hr}^{-1}$ following the replacement of BLG43 observations with BLG18 observations.

The KMTNet and LCOGT data were both reduced using the pySIS pipeline (Albrow et al. 2009; Yang et al. 2024, 2025), which is based on the difference image analysis (DIA) technique (Tomaney & Crofts 1996; Alard & Lupton 1998). The data error bars were rescaled following the method in Yee et al. (2012).

3 LIGHT-CURVE ANALYSIS

3.1 Preamble

We start from the standard 2L1S model, which is described with seven parameters. These include three point-source point-lens (PSPL, Paczynski 1986) parameters: t_0 , the time of closest lens-source alignment; u_0 the closest distance of the source to the lens center of mass in the unit of angular Einstein radius θ_E ; t_E , the Einstein radius crossing time. This timescale is related to the Einstein radius θ_E and the total lens mass M_L by:

$$t_E \equiv \frac{\theta_E}{\mu_{\text{rel}}}; \quad \theta_E \equiv \sqrt{\kappa M_L \pi_{\text{rel}}}. \quad (1)$$

Here $\kappa \equiv \frac{4G}{c^2 \text{au}} \simeq 8.144 \text{ mas}/M_\odot$, and $(\pi_{\text{rel}}, \mu_{\text{rel}})$ are the lens-source relative parallax and proper motion (Gould 2000). Another three parameters are required to describe the binary lens geometry: s , the projected planet-to-star separation in units of θ_E ; q , the planet-to-star mass ratio; and α , the angle between source trajectory and binary lens axis. The last parameter ρ is the angular size of the source, θ_* , in units of θ_E . The blending effect is described by two linear parameters for each data set i : the source flux $f_{S,i}$ and the blending flux $f_{B,i}$. The observed flux for each data set is then given by

$$F_i(t) = f_{S,i}A(t) + f_{B,i}. \quad (2)$$

For the light curve in each observational site, we first use a binary lens model to calculate the magnification and then use linear regression to determine the blending parameters.

We start the modeling process with a parameter search in a dense grid in the (s, q, α) space. At each grid point, the initial guesses for the parameters (s, q, α) are given by the values of the grid point, and values for the other parameters (t_0, u_0, t_E, ρ) are taken from the PSPL fit. The model χ^2 is minimized via

the Covariance Matrix Adaptation Evolution Strategy (CMA-ES) algorithm⁴ from `pycma` (Hansen et al. 2019). During the minimization, values of the parameters (s, q) are fixed, whereas the other parameters $(t_0, u_0, t_E, \rho, \alpha)$ are allowed to vary. The best solutions in each grid are then polished with the Nelder-Mead simplex algorithm (Nelder & Mead 1965; Gao & Han 2012) with all parameters as free. Because no model gradients are used in either optimization algorithm, we use the `VMicrolensing` (Bozza 2010; Bozza et al. 2018; Bozza et al. 2025) to compute the 2L1S magnification at this stage.

For high-magnification events, the limb-darkening effect is important for estimating the source radius. We use the linear limb-darkening law described by

$$S_\lambda(\nu) = S_\lambda(0)[1 - a_\lambda(1 - \nu)] \quad \nu = \sqrt{1 - \frac{r^2}{\rho^2}}, \quad (3)$$

where the $S_\lambda(0)$ is the surface brightness at the center of the source, r and ρ are the distance to the center of the source and the source radius, respectively, and a_λ is the limb-darkening coefficient at wavelength λ . We infer the effective temperature T_{eff} in Section 4.1 and obtain the limb-darkening coefficients based on the stellar model in Claret & Bloemen (2011).

After the locations of the probable solutions are identified from the grid search, we are then set to sample the posterior distributions of the model parameters. The 2L1S posteriors for these two high-magnification events are obtained using HMC, which is a gradient-based variant of MCMC. Compared to the traditional MCMC, HMC has several advantages, including the ability to efficiently draw samples with weaker autocorrelation while maintaining a high acceptance rate, even in high dimensions (Neal 2011). We use the `microlux` code for the 2L1S model at this stage. In the recent version 0.2.0, `microlux` adopts the new polynomial coefficient calculation of Wang et al. (2025) to boost the robustness for planetary and extreme binary cases, which will be the situation we face for the two events under consideration.

To maximize HMC performance, we utilize the local covariance obtained from the Fisher information matrix to reparameterize the binary microlensing parameters, thereby mitigating the strong correlation between certain parameters. This method has been applied in historical events modeling Ren & Zhu (2025); Miyazaki & Kawahara (2025). Here, we follow a similar scheme, which nevertheless differs in some aspects, to implement the reparameterization. Specifically, we initially draw unconstrained and uniform samples from the latent space β' , implemented by `ImproperUniform` in `Numpyro`. The uniform and unconstrained features are chosen to avoid the prior information introduced in the later reparameterization. The true parameters are given by a triangular affine transformation

$$\beta = \mu + L\beta', \quad (4)$$

where μ is the initial guess, L is a lower triangular matrix from Cholesky factorization of the covariance matrix $LL^T = \Sigma$. To constrain the transformed parameters within physical bounds without disrupting the continuous gradients required by HMC, we impose a soft-boundary penalty in likelihood via the `softplus` function. This reparameterization effectively preconditions the sampling space, equivalent to adapting the HMC mass matrix (metric) to the local covariance, thereby accelerating the warm-up phase.

For both events, the bump-type anomaly could also be caused by a 1L2S model, which can mimic the 2L1S model (Gaudi 1998). Thus, we also try to fit a 1L2S model to the data. A 1L2S model is defined

⁴ <https://github.com/CMA-ES/pycma>

with two sets of PSPL parameters, but with a common timescale, t_E , which correspond to two background source stars. The 1L2S total magnification at waveband λ , $A_\lambda(t)$, is given by (Hwang et al. 2013)

$$A_\lambda(t) = \frac{A_1(t)f_{S,1,\lambda} + A_2(t)f_{S,2,\lambda}}{f_{S,1,\lambda} + f_{S,2,\lambda}} = \frac{A_1(t) + q_{f,\lambda}A_2(t)}{1 + q_{f,\lambda}}, \quad (5)$$

where

$$q_{f,\lambda} \equiv \frac{f_{S,2,\lambda}}{f_{S,1,\lambda}} \quad (6)$$

is the ratio of the two source fluxes at wavelength λ . The quantity $A_j(t)$ represents the magnification given by the j -th source. We use `VBMicrolensing` to calculate the 1L2S model with the finite source effect.

3.2 KMT-2025-BLG-1314

Figure 1 displays the observed data of KMT-2025-BLG-1314, which has an asymmetric feature or a double-bump feature over the peak of a PSPL model.

We include the limb-darkening effect of the source with the linear limb darkening law in the modeling. As described in Section 3.1, we infer the effective temperature of $\sim 5000\text{K}$ and $\log g \sim 4.5$. Assuming the initial turbulence velocity $\sim 1\text{km/s}$ and solar metallicity, we have the $u_I = 0.562$ (Claret & Bloemen 2011). Considering the limb-darkening effect, we then investigate the local posterior around these best solutions.

For this event, the initial grids are sampled based on a reparameterization method similar to Dong et al. (2009), in order to make the grid search more efficient. The initial guesses include 40 values for caustic width $\log w$ uniformly spaced over $[-3.5, -2.0]$, 60 values for $\log q$ over $[-5.0, 2.0]$ and 10 values for α over $[0, 2\pi]$. The horizontal caustic width $\log w$ is given by the Chang & Refsdal (1984) lens approximation with different shear γ definitions and limiting regions (Chung et al. 2005; An 2005; Zhang 2023). Based on these works, a general approximation formula takes the form,

$$w = \frac{4q}{(s - s^{-1})^2(1 + q)^2} (s < s_c), \quad w = \frac{4q}{(s - s^{-1})^2(1 + q)} (s > s_w) \quad (7)$$

$$s - s^{-1} - w(s, q) + 2\frac{\gamma q^{\frac{1}{2}}}{\sqrt{1 - \gamma}} = 0; \quad (s_c < s < s_w); \quad \gamma = \left(\frac{\sqrt{w^2 + 4} + w}{2} \right)^{-2}, \quad (8)$$

where s_c and s_w denote the boundary transition point between the close, wide, and resonant caustics topology (Dominik 1999) and follows

$$s_c = \left[\frac{(1 - s_c^4)^3 (1 + q)^2}{27q} \right]^{1/8}; \quad s_w = \frac{(1 + q^{1/3})^{3/2}}{\sqrt{1 + q}}. \quad (9)$$

The grid-search results are shown in Figure 2. Similar to the three events affected by the ‘‘Planet/Binary’’ degeneracy analyzed by Zhang et al. (2026a), KMT-2025-BLG-1314 has six ‘‘Binary’’ solutions, none of which show measurable finite-source effects, as well as four planetary solutions ($\log q < -2$), among which two have measurable finite-source effects, and two do not. This situation is similar to that of KMT-2022-BLG-0954 analyzed by Zhang et al. (2026a) and OGLE-2011-BLG-0950 analyzed by Zhang et al. (2026). Following the definitions of Zhang et al. (2026a), we label these solutions as ‘‘Close Binary AB’’, ‘‘Close Binary BC’’, ‘‘Wide Binary AB’’, ‘‘Wide Binary BC’’, ‘‘Wide Binary CD’’, and ‘‘Wide Binary DA’’ for the binary solutions, and ‘‘Close Planet Point’’, ‘‘Wide Planet Point’’, ‘‘Close Planet Finite’’, and ‘‘Wide Planet

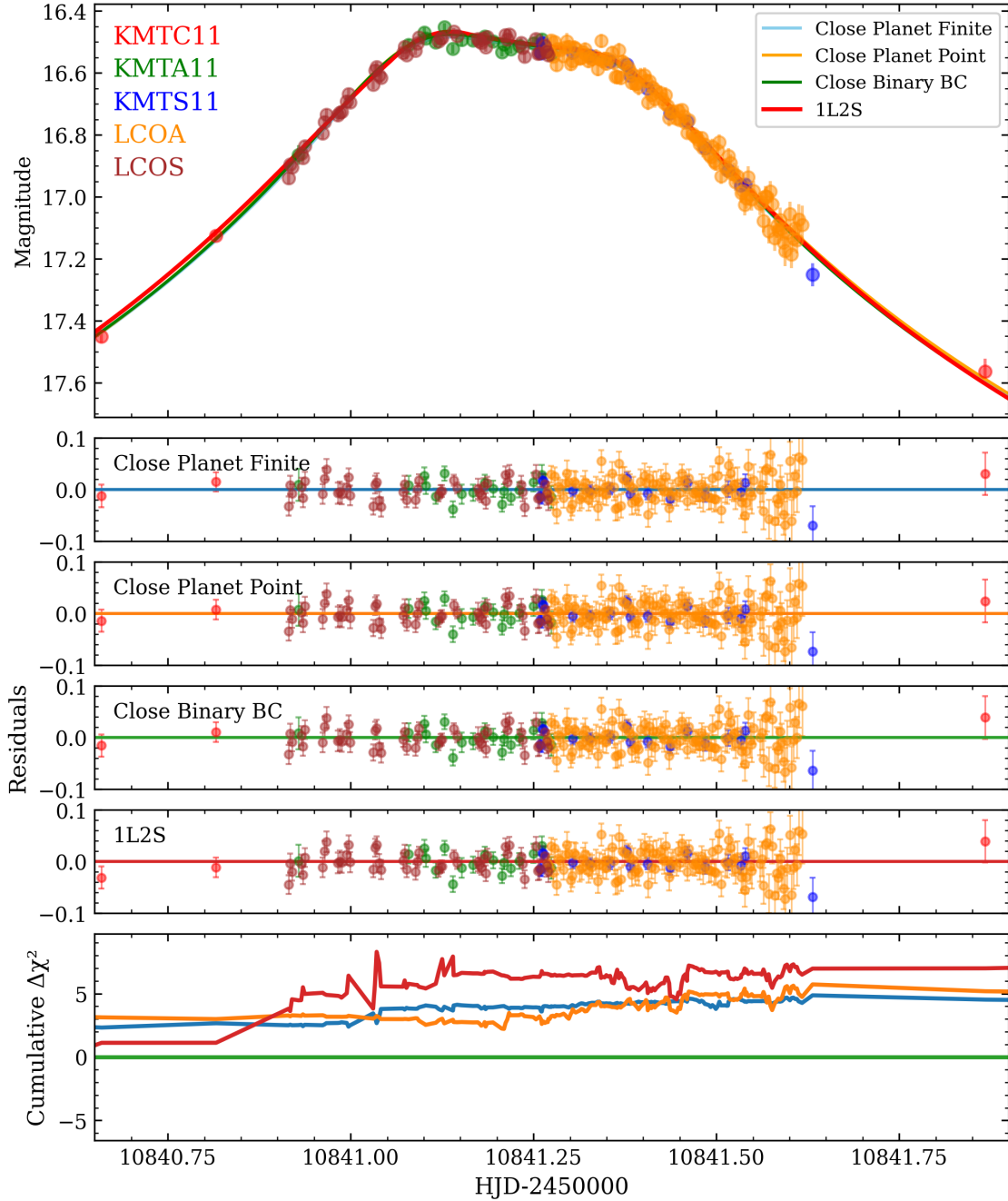


Fig. 1: Light curve and the best-fit model of the microlensing event KMT-2025-BLG-1314. Different data sets are shown in different colors. The “Close Binary BC” solution has the lowest χ^2 . The bottom panel shows the residual distribution for four different solutions relative to the “Close Binary BC” solution. Different data sets are aligned to the KMTTC11 I -band data.

Finite” for the planetary solutions. Here, “Close” denotes solutions with $s < 1$, while “Wide” denotes solutions with $s > 1$. The corresponding caustic structures and source trajectories are shown in Figure 3. We note that this event represents the third case in which “Planet Point” solutions have been identified within the “Planet/Binary” degeneracy, following its first identification by Zhang et al. (2026a) for the event KMT-2022-BLG-0954. Zhang et al. (2026b) subsequently noted the existence of these previously missed solutions in one of the earliest “Planet/Binary” events (Choi et al. 2012), thereby maintaining the viability

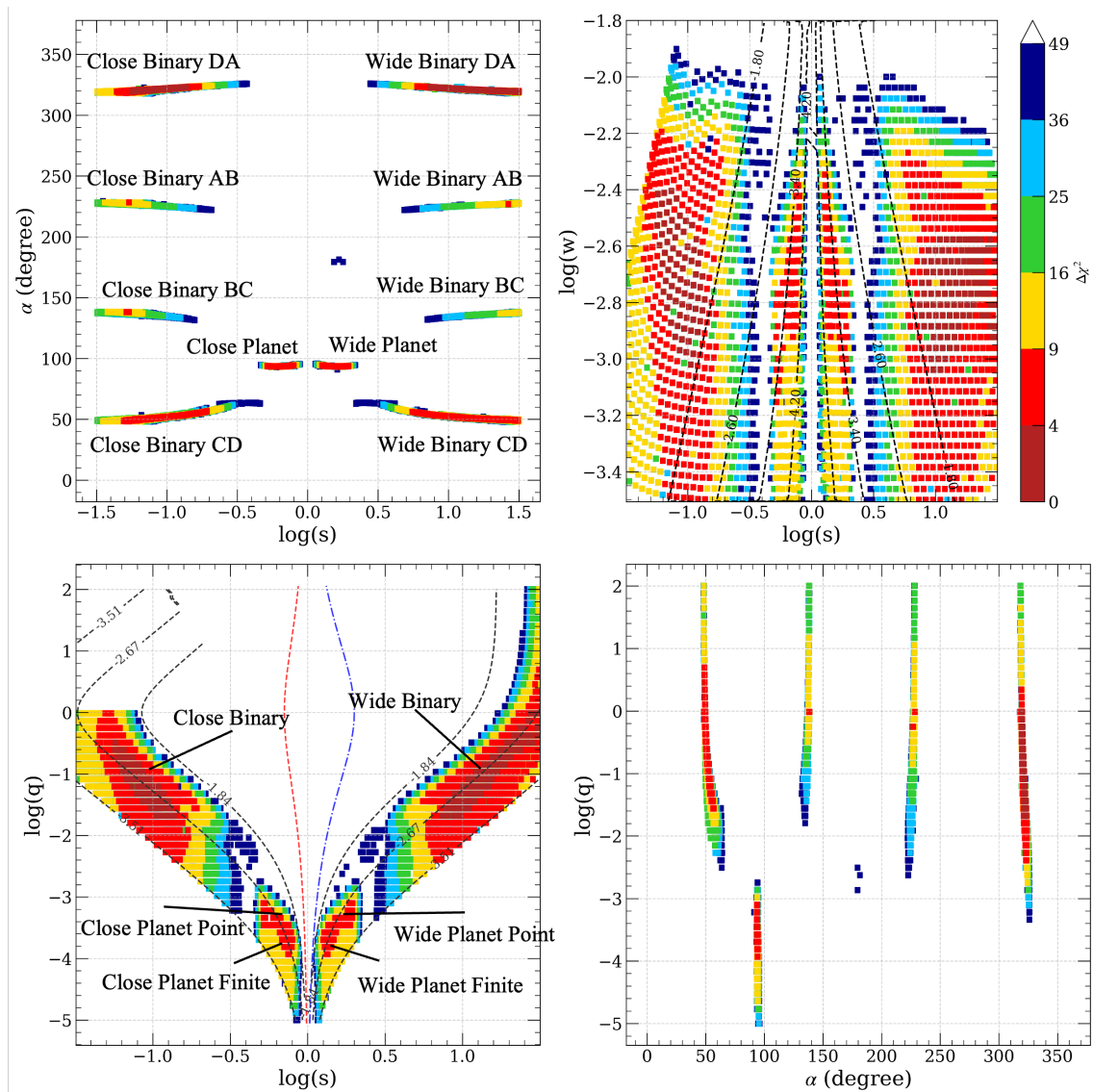


Fig. 2: The χ^2 distribution projected onto the four planes of $(\log s, \log q, \alpha, \log w)$ space from the grid search result of KMT-2025-BLG-1314. The grid points with $\Delta\chi^2 > 49$ are left blank. The different degenerate solutions are marked with their names. The gray dashed lines in the $(\log s, \log w)$ and $(\log s, \log q)$ panels represent the envelopes with constant value of $\log q$ and $\log w$, respectively. The red and blue dashed lines mark the boundaries between resonant and close/wide caustics geometries (Dominik 1999). In total, ten local minima are identified.

of the planetary interpretation when combined with Keck adaptive optics imaging (Terry et al. 2022). The discovery of the “Planet Point” solutions in the present event demonstrates that this class of solutions is a common feature of the “Planet/Binary” degeneracy.

The final best-fit parameters and their uncertainties are listed in Table 1. The modeling indicates that the “Close Binary BC” solution provides the best fit to the data, while the other nine solutions are disfavored by $\Delta\chi^2$ values ranging from 0.2 to 14.2. Given the relatively small differences in goodness of fit, we retain all 2L1S solutions and investigate their corresponding source and lens properties in the subsequent section.

We also examine the microlensing parallax effect (Gould 1992, 2000) by introducing two additional parameters, $(\pi_{E,N}, \pi_{E,E})$, which represent the north and east components of the microlensing parallax vector.

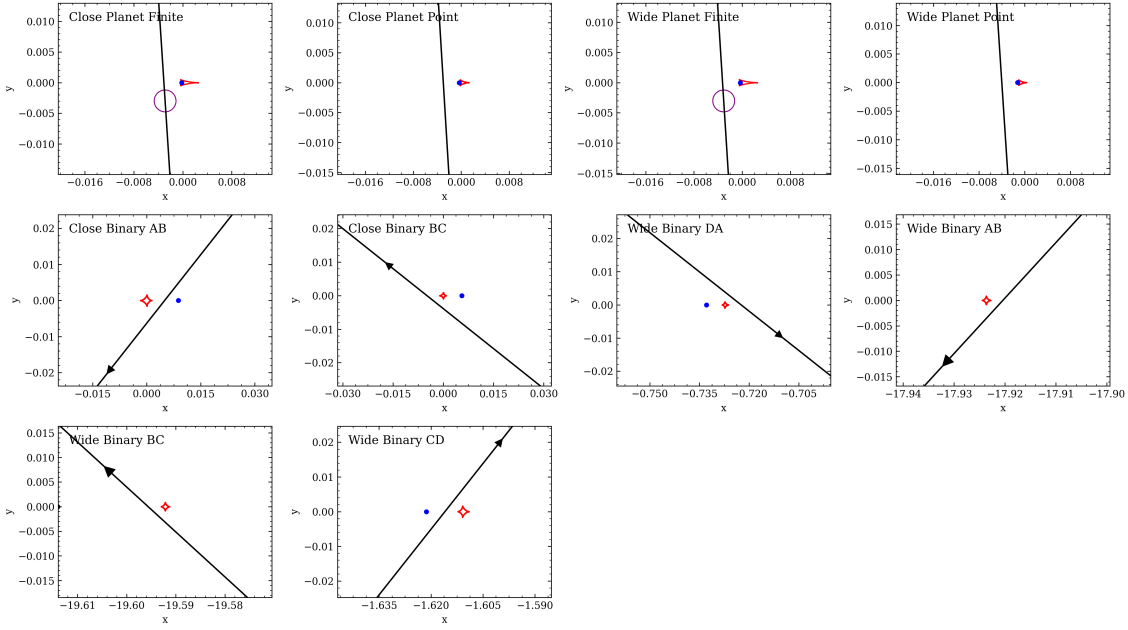


Fig. 3: Trajectory configuration of 10 solutions for KMT-2025-BLG-1314. The red curves denote the caustic geometries, the blue dots represent the position of the primary lens, and the purple circles indicate the source radii. The black lines show the source-lens relative trajectory with the arrow indicating the source motion direction. The coordinate origin is set at the magnification center. The 2L1S lensing parameters are shown in Table 1.

However, owing to the faintness of the source ($I_S > 22$), the improvement in χ^2 is < 1 , and the 1σ uncertainties in the parallax components exceed 0.5 in all directions. Consequently, no meaningful constraints on the microlensing parallax can be obtained for this event.

For the 1L2S model, the MCMC-derived parameters are listed in Table 2. The best-fit 1L2S solution is disfavored relative to the best-fit 2L1S model by $\Delta\chi^2 \sim 10$. Finite-source effects are detected for both sources. Based on the source-property analysis presented in the subsequent section, the inferred lens-source relative proper motion is $\mu_{\text{rel}} = \theta_E/t_E \sim 0.5 \text{ mas yr}^{-1}$. Using Equation (9) of Jung et al. (2022), which is derived from the observed distribution of μ_{rel} for planetary microlensing events (Gould 2022), the probability of obtaining $\mu_{\text{rel}} \leq 0.5 \text{ mas yr}^{-1}$ is only 5×10^{-4} , corresponding to an effective $\Delta\chi^2 \sim 15$. When this prior information is taken into account, the 1L2S model is disfavored by a total $\Delta\chi^2 \sim 25$. Besides the statistical disfavor, the 1L2S geometry is physically implausible. The projected separation between the two sources ($\Delta u \sim 0.0057$) is only ~ 1.1 times the sum of their radii ($\rho_1 + \rho_2 \sim 0.0052$). For typical stellar masses, this implies a contact or near-contact binary configuration, barring an improbable projection effect. Therefore, we conclude that the 1L2S interpretation is strongly disfavored and physically unrealistic for this event and thus reject the 1L2S model.

In conclusion, for KMT-2025-BLG-1314, the planetary and stellar-binary interpretations for the 2L1S model both remain viable.

Table 1: 2L1S parameters for KMT-2025-BLG-1314

Model	t_0 (HJD')	u_0	t_E (day)	α (degree)	$\log \rho$	$\log q$	$\log s$	$I_{S,KMTA}$	χ^2/dof
Close Planet Finite	10841.212	0.00315	74.004	94.124	-2.739	-3.650	-0.123	23.52	1022.7/1041
	± 0.002	± 0.00061	± 14.421	± 0.630	± 0.084	± 0.118	± 0.027	± 0.25	
Close Planet Point	10841.214	0.00310	71.424	93.494	< -2.665	-3.238	-0.255	23.61	1025.3/1041
	± 0.002	± 0.00053	± 13.211	± 0.570	—	± 0.097	± 0.024	± 0.21	
Wide Planet Finite	10841.213	0.00311	74.481	93.626	-2.742	-3.621	0.126	23.50	1022.8/1041
	± 0.002	± 0.00066	± 15.262	± 0.658	± 0.093	± 0.117	± 0.028	± 0.22	
Wide Planet Point	10841.214	0.00310	70.493	93.759	< -2.668	-3.177	0.279	23.45	1025.2/1041
	± 0.001	± 0.00053	± 13.066	± 0.582	—	± 0.096	± 0.023	± 0.18	
Close Binary AB	10841.207	0.004114	59.259	231.592	< -2.551	0.950	-1.019	23.27	1025.7/1041
	± 0.003	± 0.000769	± 12.536	± 1.344	—	± 0.375	± 0.103	± 0.16	
Close Binary BC	10841.210	0.003338	66.779	141.348	< -2.595	1.148	-1.041	23.49	1019.5/1041
	± 0.002	± 0.000570	± 13.836	± 1.105	—	± 0.296	± 0.111	± 0.18	
Wide Binary DA	10841.209	0.003174	70.599	321.384	< -2.756	-0.977	1.134	23.45	1019.7/1041
	± 0.002	± 0.000660	± 19.375	± 1.037	—	± 0.367	± 0.141	± 0.22	
Wide Binary AB	10841.217	0.002861	81.589	227.095	< -2.724	-0.094	1.417	23.28	1030.6/1041
	± 0.002	± 0.000503	± 13.418	± 0.643	—	± 0.240	± 0.064	± 0.18	
Wide Binary BC	10841.215	0.002726	87.575	137.428	< -2.617	0.168	1.440	23.24	1033.7/1041
	± 0.001	± 0.000359	± 9.735	± 0.521	—	± 0.190	± 0.033	± 0.17	
Wide Binary CD	10841.209	0.003732	64.885	50.832	< -2.613	-0.633	1.191	23.16	1025.2/1041
	± 0.002	± 0.000630	± 12.383	± 1.038	—	± 0.317	± 0.128	± 0.14	

Notes: HJD' = HJD - 2450000. The parameters are reported with 1σ uncertainties for constrained values and 3σ limit for unconstrained ρ . The coordinate origin is set at the magnification center.

Table 2: 1L2S parameters for the Two Events

Parameter	KMT-2025-BLG-1314	KMT-2025-BLG-1392
χ^2/dof	1029.8/1041	2032.3/1791
$t_{0,1}$ (day)	10841.107 ± 0.004	10845.177 ± 0.00019
$t_{0,2}$ (day)	10841.358 ± 0.004	10845.024 ± 0.005
$u_{0,1}$	0.00276 ± 0.00068	0.00145 ± 0.00009
$u_{0,2}$	-0.00236 ± 0.00070	-0.01460 ± 0.00136
t_E (day)	96.34 ± 18.86	17.52 ± 1.34
$\log \rho_1$	-2.553 ± 0.108	...
$\log \rho_2$	-2.627 ± 0.148	< -1.80
q_1	0.611 ± 0.097	2.808 ± 0.100

3.3 KMT-2025-BLG-1392

As shown in Figure 4, the light curve of KMT-2025-BLG-1392 exhibits a ~ 3 -hour bump following the PSPL peak. The anomaly is mainly densely covered by LCOA01, LCOA02, and KMTA data. The adopted limb-darkening coefficient is $u_I = 0.582$ with an effective temperature of $\sim 4800\text{K}$. The parameter search for KMT-2025-BLG-1392 begins with a $(40 \times 40 \times 10)$ grid spanning the ranges $\log s \in [-1, 0.7]$, $\log q \in [-5, 0]$, and $\alpha \in [0, 2\pi]$. From the grid-search results, we identify two local minima corresponding to the well-known ‘‘Close/Wide’’ degeneracy (Griest & Safizadeh 1998; Dominik 1999; An 2005). The MCMC results with all parameters free are listed in Table 3. The ‘‘Wide’’ solution provides the best fit to the data,

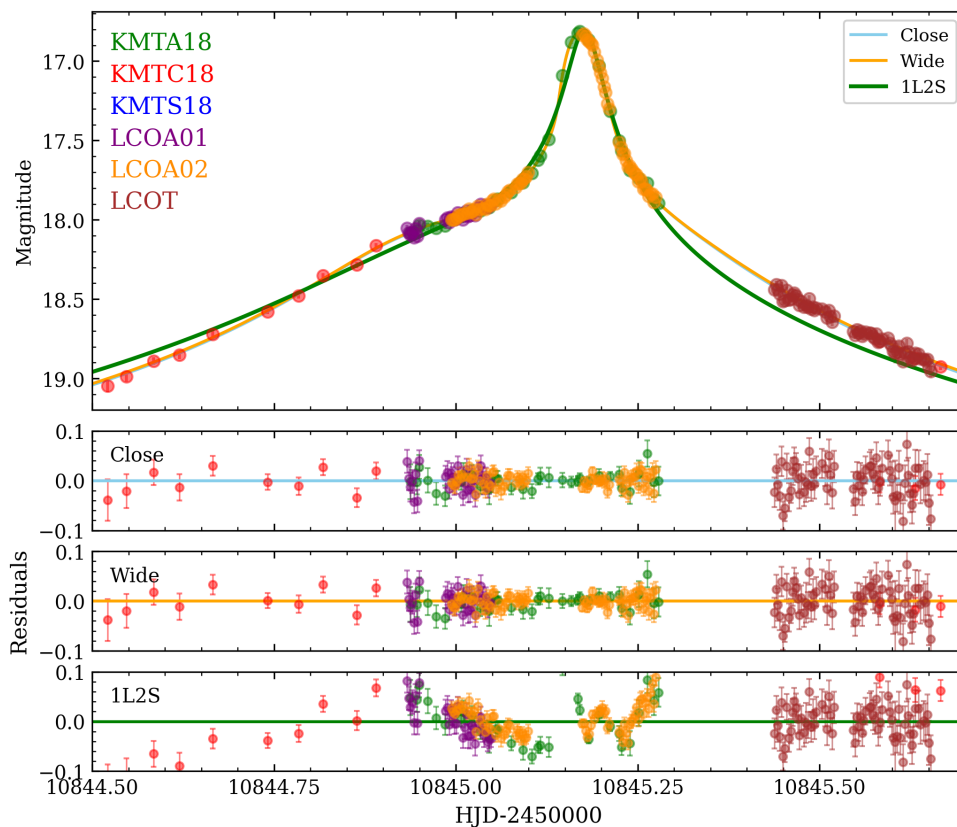


Fig. 4: Light curve and the best-fit model of the microlensing event KMT-2025-BLG-1392. The bottom panel shows the residual distribution for the 2L1S close/wide solutions and the 1L2S solution. Note that the multi-site data in the top panel are aligned to the KMTA scale using the source and blend fluxes (f_s , f_b) of the “Close” model. Because the 1L2S model has a significantly different χ^2 and requires different flux parameters, its model curve shows an apparent visual offset from the aligned data. The residuals in the bottom panels, however, are computed independently using each model’s respective best-fit flux parameters.

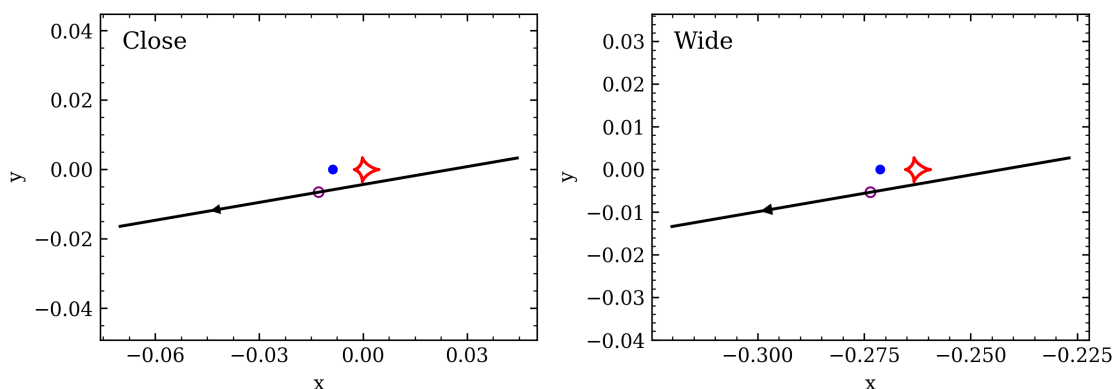


Fig. 5: Trajectory configuration of the event KMT-2025-BLG-1392.

while the “Close” solution is disfavored by only $\Delta\chi^2 = 0.2$. Figure 5 shows the caustic geometry and the source trajectory, from which it is clear that the anomaly is produced by a source crossing the central caustic.

Table 3: 2L1S Parameters for KMT-2025-BLG-1392

Solution	Close	Wide
χ^2/dof	1786.2/1791	1786.0/1791
$t_0(\text{day})$	10845.145 ± 0.001	10845.146 ± 0.001
u_0	0.00424 ± 0.00052	0.00422 ± 0.00050
$t_E(\text{day})$	25.906 ± 3.204	25.953 ± 3.477
α (degree)	189.866 ± 0.321	189.791 ± 0.318
$\log \rho$	-2.860 ± 0.052	-2.860 ± 0.055
q	0.0434 ± 0.0078	0.0519 ± 0.0103
$\log s$	-0.691 ± 0.019	0.733 ± 0.022
$I_{S,\text{KMTC}}$	22.33 ± 0.14	22.32 ± 0.13

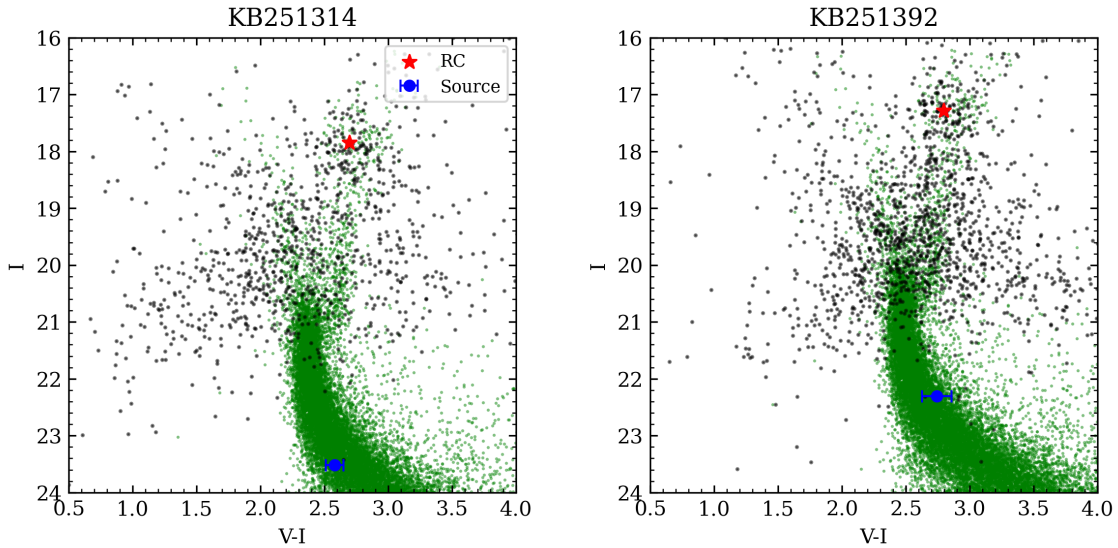


Fig. 6: Color magnitude diagram for the two events, constructed from the KMT field stars $120''$ square centered on the event position (KMTA for KMT-2025-BLG-1314 and KMTC data for KMT-2025-BLG-1392). The red star marker represents the centroid of the red clump, and the blue dot shows the inferred position of the source star from the best-fit 2L1S model. The green dots represent the HST CMD of Holtzman et al. (1998) whose red-clump centroid has been matched to that of KMT using $(V - I, I)_{\text{cl,HST}} = (1.62, 15.15)$ (Bennett et al. 2008).

As shown in Table 2 and Figure 4, the 1L2S model fails to reproduce the anomaly and is disfavored relative to the 2L1S model by $\Delta\chi^2 = 246$. We therefore reject the 1L2S interpretation for this event.

With $q \sim 0.05$, the primary lens is inferred to host a companion near the planet/brown-dwarf boundary.

4 SOURCE AND LENS PROPERTIES

4.1 Color-Magnitude Diagram

To measure the angular radius of the source star, θ_* , thus to obtain the angular Einstein radius through $\theta_E = \theta_*/\rho$, we locate the source star on a color-magnitude diagram (CMD). For both events, the CMD is constructed using the star from the KMT field stars located $120''$ square centered on the event position

Table 4: 2LIS source properties and derived θ_E and μ_{rel} for KMT-2025-BLG-1314.

Model	$(V - I, I)_{S, \text{KMTA}}$	$(V - I, I)_{S, 0}$	θ_* (μas)	θ_E (mas)	μ_{rel} (mas yr^{-1})
Close Planet Finite	2.58 ± 0.07	0.95 ± 0.08	0.36 ± 0.05	0.198 ± 0.048	0.98 ± 0.30
	23.52 ± 0.25	20.26 ± 0.27			
Close Planet Point	2.58 ± 0.07	0.95 ± 0.08	0.35 ± 0.04	> 0.161	> 0.82
	23.61 ± 0.21	20.35 ± 0.23			
Wide Planet Finite	2.58 ± 0.07	0.95 ± 0.08	0.37 ± 0.05	0.202 ± 0.051	0.99 ± 0.32
	23.50 ± 0.22	20.24 ± 0.24			
Wide Planet Point	2.58 ± 0.07	0.95 ± 0.08	0.37 ± 0.04	> 0.174	> 0.90
	23.45 ± 0.18	20.19 ± 0.21			
Close Binary AB	2.58 ± 0.07	0.95 ± 0.08	0.41 ± 0.05	> 0.144	> 0.89
	23.27 ± 0.16	20.01 ± 0.19			
Close Binary BC	2.58 ± 0.07	0.95 ± 0.08	0.37 ± 0.04	> 0.144	> 0.79
	23.49 ± 0.18	20.23 ± 0.21			
Wide Binary DA	2.58 ± 0.07	0.95 ± 0.08	0.37 ± 0.05	> 0.213	> 1.10
	23.45 ± 0.22	20.19 ± 0.24			
Wide Binary AB	2.58 ± 0.07	0.95 ± 0.08	0.40 ± 0.05	> 0.214	> 0.96
	23.28 ± 0.18	20.02 ± 0.21			
Wide Binary BC	2.58 ± 0.07	0.95 ± 0.08	0.41 ± 0.05	> 0.170	> 0.71
	23.24 ± 0.17	19.98 ± 0.20			
Wide Binary CD	2.58 ± 0.07	0.95 ± 0.08	0.43 ± 0.05	> 0.175	> 0.99
	23.16 ± 0.14	19.90 ± 0.17			

Notes: The position of the red clump centroid is estimated to be $(V - I, I)_{\text{RC, KMTA}} = (2.694 \pm 0.025, 17.850 \pm 0.099)$, and its intrinsic position is $(V - I, I)_{\text{RC, 0}} = (1.06 \pm 0.03, 14.59 \pm 0.04)$ (Bensby et al. 2013; Nataf et al. 2013).

(KMTA for KMT-2025-BLG-1314 and KMTC data for KMT-2025-BLG-1392). Following the method in Nataf et al. (2013), we first determine the centroid of the red clump (RC), $(V - I, I)_{(\text{RC}, 0)}$. From Bensby et al. (2013) and Table 1 of Nataf et al. (2013), we obtain the de-reddened color and magnitude of the RC, $(V - I, I)_{\text{RC}, 0}$. The source I -band apparent magnitude is derived from the light-curve modeling. The source color, $(V - I)_S$, is calculated based on the linear regression between the I -band and V -band light curve data. Then, the source de-reddened color and magnitude can be derived by

$$(V - I, I)_{S, 0} = (V - I, I)_S - [(V - I, I)_{\text{RC}} - (V - I, I)_{\text{RC}, 0}]. \quad (10)$$

We apply the empirical color–surface brightness relation of Adams et al. (2018) to obtain the source angular size θ_* . The derived parameters from the above processes, and the inferred θ_E and μ_{rel} for different solutions are listed in Table 4 and Table 5. We also estimate the effective temperature T_{eff} of the source (Houdashelt et al. 2000) to determine the limb-darkening coefficients used in Sec 3.

4.2 Bayesian Analysis

To determine lens properties in the absence of parallax measurements, we use a Bayesian analysis to incorporate a prior from the galactic model. We follow the basic procedure of (Zhu et al. 2017). The differential

Table 5: 2LIS source properties and derived θ_E and μ_{rel} for KMT-2025-BLG-1392.

Model	$(V - I, I)_{S, \text{KMTTC}}$	$(V - I, I)_{S, 0}$	$\theta_*(\mu\text{as})$	$\theta_E(\text{mas})$	$\mu_{\text{rel}}(\text{mas yr}^{-1})$
Close	2.74 ± 0.12	1.01 ± 0.12	0.56 ± 0.07	0.407 ± 0.071	5.74 ± 1.23
	22.33 ± 0.14	19.42 ± 0.15			
Wide	2.74 ± 0.12	1.01 ± 0.12	0.56 ± 0.07	0.409 ± 0.073	5.75 ± 1.28
	22.32 ± 0.13	19.41 ± 0.14			

Notes: The position of the red clump centroid is estimated to be $(V - I, I)_{\text{RC, KMTTC}} = (2.798 \pm 0.017, 17.284 \pm 0.054)$, and its intrinsic position is $(V - I, I)_{\text{RC, 0}} = (1.06 \pm 0.03, 14.38 \pm 0.04)$.

event rate of the galactic model at a certain source distance D_S is given by

$$\frac{d^3\Gamma}{dD_L d\log M_L d\mu_{\text{rel}}} = 4\pi n_{L,*} D_L^2 \theta_E^2 \mu_{\text{rel}}^2 f_\mu(\mu_{\text{rel}}) \frac{d\xi(M_L)}{d\log M_L}, \quad (11)$$

where $n_{L,*}$ is the local stellar density given the galactic coordinates, $f_\mu(\mu_{\text{rel}})$ is the probability distribution function for the norm of the lens-source relative proper motion μ_{rel} , the M_L and D_L are the lens mass and lens distance, respectively. For the lens mass distribution, we use the present-day mass function, which combines the initial mass function of Kroupa (2001) at the low-mass end and the mass function for stellar remnants. The mass functions for stellar remnants are adopted from Gentile Fusillo et al. (2019) for white dwarfs, Kiziltan et al. (2013) for neutron stars, and Olejak et al. (2020) for black holes. For the galactic model, we use the prescription in Zhu et al. (2017).

Because all the event solutions yield no parallax constraints, we use the θ_E and μ_{rel} measurements to constrain the posterior. The marginal probability distributions for D_L and M_L , given certain θ_E and μ_{rel} measurements, are derived as follows:

$$\frac{d^3\Gamma}{dD_L d\theta_E d\mu_{\text{rel}}} = \frac{d^3\Gamma}{dD_L d\log M_L d\mu_{\text{rel}}} \left| \frac{\partial(D_L, \log M_L, \mu_{\text{rel}})}{\partial(D_L, \theta_E, \mu_{\text{rel}})} \right| \propto n_{L,*} D_L^2 \mu_{\text{rel}}^2 f_\mu(\mu_{\text{rel}}) \frac{d\xi(M_L)}{d\log M_L}, \quad (12)$$

and

$$\frac{d^3\Gamma}{dM_L d\theta_E d\mu_{\text{rel}}} = \frac{d^3\Gamma}{dD_L d\log M_L d\mu_{\text{rel}}} \left| \frac{\partial(D_L, \log M_L, \mu_{\text{rel}})}{\partial(M_L, \theta_E, \mu_{\text{rel}})} \right| \propto n_{L,*} D_L^4 \theta_E^2 \mu_{\text{rel}}^2 M_L^{-1} f_\mu(\mu_{\text{rel}}) \frac{d\xi(M_L)}{d\log M_L}. \quad (13)$$

The marginalized probability of distance can be obtained by integrating the posterior samples from the MCMC chain, i.e, for each sample in the MCMC chains, we calculate the $(\theta_E, \mu_{\text{rel}})$ based on the parameters $(t_E, \log \rho, \theta_*)$ and subsequently calculate the marginal distribution of lens mass and lens distance. This gives

$$\frac{d\Gamma}{D_L} \propto \int \frac{d^3\Gamma}{dD_L d\theta_E d\mu_{\text{rel}}} p(\theta_E, \mu_{\text{rel}} | \text{Data}) d\theta_E d\mu_{\text{rel}} = \sum_{i \sim \text{MCMC samples}} \frac{d^3\Gamma}{dD_L d\theta_{E,i} d\mu_{\text{rel},i}}. \quad (14)$$

Although the finite source effects are not rigorously detected for ‘‘Planet Point’’ and ‘‘Binary’’ solutions of KMT-2025-BLG-1314, we still use the posterior samples from the MCMC chain with the cut of $\log \rho \in [-4, -2]$ to avoid unreasonable $(\theta_E, \mu_{\text{rel}})$ combinations. We also consider the variation in D_S by integration the probability distribution function over all possible values from $D_{\text{min}} = 6$ kpc to $D_{\text{max}} = 10$ kpc with the probability weight $D_S^{2-\gamma}$ ($\gamma = 2.85$) according to the local stellar density (Zhu et al. 2017).

4.3 KMT-2025-BLG-1314

For KMT-2025-BLG-1314, the source is likely a K dwarf in the Galactic bulge. For the two ‘‘Planet Finite’’ solutions, the lens-source relative proper motion are both low, with $\mu_{\text{rel}} \sim 1$ mas yr $^{-1}$, for which the values

Table 6: Physical Parameters Derived from Bayesian Analysis for KMT-2025-BLG-1314.

Model	D_L (kpc)	M_1 (M_\odot)	M_2	r_\perp (AU)
Close Planet Finite	$8.08^{+0.59}_{-0.76}$	$0.38^{+0.32}_{-0.19}$	$0.088^{+0.078}_{-0.051} M_{\text{Jup}}$	$1.21^{+0.31}_{-0.32}$
Close Planet Point	$7.57^{+0.74}_{-1.69}$	$0.61^{+0.36}_{-0.30}$	$0.37^{+0.23}_{-0.20} M_{\text{Jup}}$	$2.14^{+1.54}_{-1.60}$
Wide Planet Finite	$8.09^{+0.61}_{-0.76}$	$0.39^{+0.31}_{-0.20}$	$0.097^{+0.083}_{-0.055} M_{\text{Jup}}$	$2.18^{+0.59}_{-0.60}$
Wide Planet Point	$7.44^{+0.81}_{-2.19}$	$0.64^{+0.36}_{-0.31}$	$0.45^{+0.27}_{-0.24} M_{\text{Jup}}$	$8.52^{+6.25}_{-6.67}$
Close Binary AB	$7.77^{+0.67}_{-1.04}$	$0.48^{+0.32}_{-0.25}$	$0.054^{+0.055}_{-0.050} M_\odot$	$0.41^{+0.42}_{-0.42}$
Close Binary BC	$7.67^{+0.74}_{-1.32}$	$0.54^{+0.33}_{-0.26}$	$0.039^{+0.034}_{-0.031} M_\odot$	$0.69^{+0.58}_{-0.59}$
Wide Binary DA	$6.56^{+1.31}_{-3.69}$	$0.67^{+0.34}_{-0.31}$	$0.071^{+0.065}_{-0.063} M_\odot$	$92.0^{+81.3}_{-94.6}$
Wide Binary AB	$7.41^{+0.82}_{-2.60}$	$0.36^{+0.22}_{-0.19}$	$0.29^{+0.19}_{-0.16} M_\odot$	$197.9^{+177.6}_{-189.5}$
Wide Binary BC	$7.60^{+0.79}_{-1.60}$	$0.34^{+0.23}_{-0.19}$	$0.23^{+0.16}_{-0.13} M_\odot$	$92.9^{+81.6}_{-83.4}$
Wide Binary CD	$7.90^{+0.66}_{-0.95}$	$0.39^{+0.29}_{-0.21}$	$0.091^{+0.086}_{-0.072} M_\odot$	$72.1^{+71.6}_{-71.8}$

Table 7: Physical Parameters Derived from Bayesian Analysis for KMT-2025-BLG-1392.

Model	D_L (kpc)	M_1 (M_\odot)	M_2	r_\perp (AU)
Close	$6.89^{+0.61}_{-0.88}$	$0.68^{+0.31}_{-0.27}$	$30.8^{+15.2}_{-13.2} M_{\text{Jup}}$	$0.57^{+0.11}_{-0.13}$
Wide	$6.82^{+0.63}_{-0.92}$	$0.69^{+0.31}_{-0.27}$	$37.7^{+18.5}_{-16.5} M_{\text{Jup}}$	$15.1^{+3.1}_{-3.5}$

are similar to the other two cases that show have both ‘‘Planet Finite’’ and ‘‘Planet Point’’ solutions (Zhang et al. 2026a,b). The ‘‘Planet Finite’’ solutions can be verified by future high-resolution imaging by measuring the lens-source proper motions when the lens and the source are resolved.

The physical parameters derived from the Bayesian analysis for KMT-2025-BLG-1314 are summarized in Table 6, including the component lens masses, lens distances, and the projected separations between the lens components. For the ‘‘Planet Finite’’ solutions, the secondary lens component has a sub-Saturn mass. For the ‘‘Planet Point’’ solutions, the companion mass is comparable to that of Saturn. The planet is located near the snowline for the ‘‘Close’’ solutions and well beyond the snowline for the ‘‘Wide’’ solutions according to the model $a_{\text{SL}} = 2.7(M/M_\odot)$ (Kennedy & Kenyon 2008). For the ‘‘Binary’’ solutions, the secondary lens component falls in the brown-dwarf or M-dwarf mass range, while the primary lens component is an M- or K-dwarf. The lens system is preferentially located in the Galactic bulge.

4.4 KMT-2025-BLG-1392

The source of KMT-2025-BLG-1392 is probably a G-dwarf in the Galactic bulge. The measured finite-source effects yield $\theta_E \sim 0.4$ mas and $\mu_{\text{rel}} \sim 6$ mas yr $^{-1}$, which are typical values for Galactic microlensing events. The physical parameters are listed in Table 7. Both the ‘‘Close’’ and ‘‘Wide’’ solutions indicate a similar system configuration: a low-mass brown dwarf or (possibly) a massive gas giant orbiting a K- or M-type host star in the Galactic bulge. For the ‘‘Close’’ solution, the companion lies inside the snowline, whereas for the ‘‘Wide’’ solution it is located well beyond the snowline.

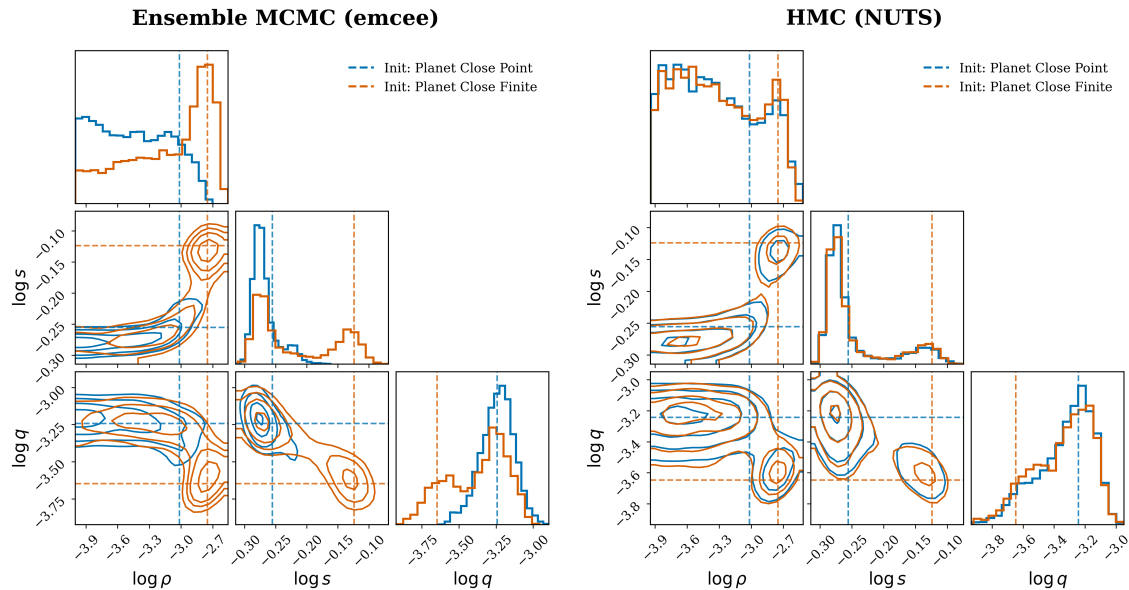


Fig. 7: Comparison of posterior sampling between ensemble MCMC sampler (`emcee`) (left panel) and HMC (NUTS, right panel) for the bimodal posterior of KMT-2025-BLG-1314. The corner plots show the 1D and 2D marginalized posterior distributions for parameters $(\log \rho, \log s, \log q)$. In each panel, two independent chains were initialized at different modes: “Planet Close Point” (blue) and “Planet Close Finite” (orange), with starting values indicated by dashed lines. Left: The `emcee` chains fail to converge to a common posterior distribution within the allotted steps. The resulting samples are strongly dependent on their initialization points, indicating poor mixing between modes due to the strong autocorrelation. Right: In contrast, the HMC chains successfully converge to identical posterior distributions regardless of the initialization point. The perfect overlap of contours and histograms demonstrates the robustness and sampling efficiency of HMC in exploring multi-modal landscapes.

5 DISCUSSION

In this work, we present the first application of differentiable modeling (e.g., HMC) to binary microlensing events enabled by `microlux`. In the modeling, the event KMT-2025-BLG-1314 exhibits a sub-degeneracy for the “Planet” solutions characterized by two distinct local minima in the posterior. This poses a challenge for the traditional MCMC method, which is prone to becoming trapped in a certain mode due to strong autocorrelation. Although HMC is not designed for dealing with multimodal posterior, we show that HMC can outperform traditional MCMC because of its weaker autocorrelation during the sampling.

Leveraging the aforementioned Fisher matrix reparameterization procedure in Section 3.1, we showcase the divergent behaviors between HMC and ensemble MCMC on sampling the bimodal distribution of KMT-2025-BLG-1314. Figure 7 shows the comparison between NUTS in HMC (`Numpyro`) (Bingham et al. 2019; Phan et al. 2019) and the affine-invariant ensemble sampler of MCMC (`emcee`) (Foreman-Mackey et al. 2013). For each sampling method, we initialize the sampler at different modes to test whether the sampler can overcome the potential barrier and reveal the true posterior. The result indicates that the HMC samples with different initial points show a consistent posterior distribution, while the MCMC samples show discrepancy. This inconsistency arises because the ensemble sampler fails to mix effectively

between the separated modes. This lack of convergence can be quantitatively diagnosed using the Gelman-Rubin statistic, \hat{R} (Gelman & Rubin 1992; Vehtari et al. 2021), which compares the parameter covariance consistency between and within chains. For the case shown in Figure 7, $\hat{R} \sim 1.3$ for `emcee` results and $\hat{R} = 1$ for HMC results. The MCMC chain samples are collected with 40 walkers, 2000 warm-up steps, and 4000 sample steps for each chain. The HMC chain samples are collected with 1 chain, 1000 warm-up steps, 4000 sample steps, and 0.9 target acceptance probability.

The above case demonstrates that HMC outperforms traditional MCMC in sampling more complex posterior distributions, even though HMC itself may not work for all types of multi-modal posteriors. For the more complicated situations, other advanced sampling algorithms are needed, such as the tempering method, Sequential Monte Carlo, and Nested sampling. The implementation of these algorithms will also benefit from a differentiable model such as `microlux`. The new modeling paradigm enabled by such differentiable models may play a crucial role in the upcoming microlensing datasets from next-generation surveys.

Acknowledgements This work is supported by the National Natural Science Foundation of China (grant Nos. 12133005 and 12173021). This research has made use of the KMTNet system operated by the Korea Astronomy and Space Science Institute (KASI) at three host sites of CTIO in Chile, SAAO in South Africa, and SSO in Australia. Data transfer from the host site to KASI was supported by the Korea Research Environment Open NETwork (KREONET). This research was supported by KASI under the R&D program (project No. 2025-1-830-05) supervised by the Ministry of Science and ICT. H.Y. acknowledges support by the China Postdoctoral Science Foundation (No. 2024M762938). Work by J.C.Y. acknowledges support from N.S.F Grant No. AST-2108414. Work by C.H. was supported by the grants of the National Research Foundation of Korea (2019R1A2C2085965 and 2020R1A4A2002885). Y.S. acknowledges support from BSF Grant No. 2020740. This work is part of the ET space mission, which is funded by China’s Space Origins Exploration Program. The authors acknowledge the Tsinghua Astrophysics High-Performance Computing platform at Tsinghua University for providing computational and data storage resources that have contributed to the research results reported within this paper.

References

- Adams, A. D., Boyajian, T. S., & von Braun, K. 2018, *MNRAS*, 473, 3608 13
- Alard, C., & Lupton, R. H. 1998, *ApJ*, 503, 325 4
- Albrow, M. D., Horne, K., Bramich, D. M., et al. 2009, *MNRAS*, 397, 2099 4
- An, J. H. 2005, *MNRAS*, 356, 1409 2, 6, 10
- Bartolić, F. 2023, *Probabilistic Modelling of Astrophysical Time Series : Gravitational Microlensing and Occultation Mapping of Planets and Moons*, Thesis, The University of St Andrews 3
- Bennett, D. P., Bond, I. A., Udalski, A., et al. 2008, *ApJ*, 684, 663 12
- Bensby, T., Yee, J. C., Feltzing, S., et al. 2013, *A&A*, 549, A147 13
- Bezanson, J., Edelman, A., Karpinski, S., & Shah, V. B. 2017, *SIAM Review*, 59, 65 3
- Bingham, E., Chen, J. P., Jankowiak, M., et al. 2019, *J. Mach. Learn. Res.*, 20, 28:1 16

- Bozza, V. 2010, MNRAS, 408, 2188 3, 5
- Bozza, V. 2024, A&A, 688, A83 2
- Bozza, V., Bachelet, E., Bartolić, F., et al. 2018, MNRAS, 479, 5157 3, 5
- Bozza, V., Saggese, V., Covone, G., Rota, P., & Zhang, J. 2025, A&A, 694, A219 3, 5
- Bradbury, J., Frostig, R., Hawkins, P., et al. 2018, JAX: composable transformations of Python+NumPy programs 3
- Brown, T. M., Baliber, N., Bianco, F. B., et al. 2013, PASP, 125, 1031 3
- Cabezas, A., Corenflos, A., Lao, J., & Louf, R. 2024, BlackJAX: Composable Bayesian inference in JAX, arXiv:2402.10797 3
- Carpenter, B., Gelman, A., Hoffman, M. D., et al. 2017, Journal of Statistical Software, 76, 1 3
- Chang, K., & Refsdal, S. 1984, A&A, 132, 168 6
- Choi, J. Y., Shin, I. G., Han, C., et al. 2012, ApJ, 756, 48 7
- Christiansen, J. L., McElroy, D. L., Harbut, M., et al. 2025, Planetary Science Journal, 6, 186 2
- Chung, S.-J., Han, C., Park, B.-G., et al. 2005, ApJ, 630, 535 6
- Claret, A., & Bloemen, S. 2011, A&A, 529, A75 5, 6
- Dominik, M. 1999, A&A, 349, 108 2, 6, 8, 10
- Dong, S., Bond, I. A., Gould, A., et al. 2009, ApJ, 698, 1826 6
- Duane, S., Kennedy, A. D., Pendleton, B. J., & Roweth, D. 1987, Physics Letters B, 195, 216 2
- Foreman-Mackey, D., Hogg, D. W., Lang, D., & Goodman, J. 2013, PASP, 125, 306 16
- Gao, F., & Han, L. 2012, Computational Optimization and Applications, 51, 259 5
- Gaudi, B. S. 1998, ApJ, 506, 533 5
- Gaudi, B. S., & Gould, A. 1997, ApJ, 486, 85 2
- Gaudi, B. S., Bennett, D. P., Udalski, A., et al. 2008, Science, 319, 927 2
- Ge, J., Zhang, H., Zang, W., et al. 2022, arXiv e-prints, arXiv:2206.06693 2
- Gelman, A., & Rubin, D. B. 1992, Statistical Science, 7, 457 17
- Gentile Fusillo, N. P., Tremblay, P.-E., Gänsicke, B. T., et al. 2019, MNRAS, 482, 4570 14
- Gould, A. 1992, ApJ, 392, 442 2, 8
- Gould, A. 2000, ApJ, 542, 785 4, 8
- Gould, A. 2022, arXiv e-prints, arXiv:2209.12501 9
- Gould, A., & Loeb, A. 1992, ApJ, 396, 104 2
- Gould, A., Zang, W.-C., Mao, S., & Dong, S.-B. 2021, Research in Astronomy and Astrophysics, 21, 133 2
- Gould, A., Jung, Y. K., Hwang, K.-H., et al. 2022, Journal of Korean Astronomical Society, 55, 173 2
- Griest, K., & Hu, W. 1992, ApJ, 397, 362 2
- Griest, K., & Safizadeh, N. 1998, ApJ, 500, 37 2, 10
- Hansen, N., Akimoto, Y., & Baudis, P. 2019, CMA-ES/pycma on Github, Zenodo, DOI:10.5281/zenodo.2559634 5
- Hoffman, M. D., & Gelman, A. 2011, arXiv e-prints, arXiv:1111.4246 2
- Holtzman, J. A., Watson, A. M., Baum, W. A., et al. 1998, AJ, 115, 1946 12
- Houdashelt, M. L., Bell, R. A., & Sweigart, A. V. 2000, AJ, 119, 1448 13

- Hwang, K. H., Choi, J. Y., Bond, I. A., et al. 2013, *ApJ*, 778, 55 6
- Jung, Y. K., Zang, W., Han, C., et al. 2022, *AJ*, 164, 262 9
- Kennedy, G. M., & Kenyon, S. J. 2008, *ApJ*, 673, 502 15
- Kim, D.-J., Kim, H.-W., Hwang, K.-H., et al. 2018a, *AJ*, 155, 76 3
- Kim, H.-W., Hwang, K.-H., Shvartzvald, Y., et al. 2018b, arXiv e-prints, arXiv:1806.07545 3
- Kim, S.-L., Lee, C.-U., Park, B.-G., et al. 2016, *Journal of Korean Astronomical Society*, 49, 37 2
- Kiziltan, B., Kottas, A., De Yoreo, M., & Thorsett, S. E. 2013, *ApJ*, 778, 66 14
- Kroupa, P. 2001, *MNRAS*, 322, 231 14
- Lam, C. Y., Lu, J. R., Udalski, A., et al. 2022, *ApJ*, 933, L23 2
- Li, H., Zhang, J., Han, C., et al. 2026, *AJ*, 171, 41 3
- Liebig, C., D'Ago, G., Bozza, V., & Dominik, M. 2015, *MNRAS*, 450, 1565 2
- Mao, S., & Paczynski, B. 1991, *ApJ*, 374, L37 2
- Miyazaki, S., & Kawahara, H. 2025, arXiv e-prints, arXiv:2510.02639 3, 5
- Mróz, P., Udalski, A., & Gould, A. 2022, *ApJ*, 937, L24 2
- Mróz, P., , A., Skowron, J., et al. 2017, *Nature*, 548, 183 2
- Nataf, D. M., Gould, A., Fouqué, P., et al. 2013, *ApJ*, 769, 88 13
- Neal, R. 2011, in *Handbook of Markov Chain Monte Carlo*, ed. S. Brooks, A. Gelman, G. Jones, & X.-L. Meng, Vol. 20116022 (Chapman and Hall/CRC), 116–62 2, 5
- Nelder, J. A., & Mead, R. 1965, *The Computer Journal*, 7, 308 5
- Olejak, A., Belczynski, K., Bulik, T., & Sobolewska, M. 2020, *A&A*, 638, A94 14
- Paczynski, B. 1986, *ApJ*, 304, 1 4
- Penny, M. T., Gaudi, B. S., Kerins, E., et al. 2019, *ApJS*, 241, 3 2
- Phan, D., Pradhan, N., & Jankowiak, M. 2019, arXiv preprint arXiv:1912.11554 3, 16
- Ren, H., & Zhu, W. 2025, *AJ*, 169, 170 3, 5
- Sahu, K. C., Anderson, J., Casertano, S., et al. 2022, *ApJ*, 933, 83 2
- Sako, T., Sekiguchi, T., Sasaki, M., et al. 2008, *Experimental Astronomy*, 22, 51 2
- Shvartzvald, Y., Maoz, D., Udalski, A., et al. 2016, *MNRAS*, 457, 4089 2
- Sumi, T., Koshimoto, N., Bennett, D. P., et al. 2023, *AJ*, 166, 108 2
- Terry, S. K., Bennett, D. P., Bhattacharya, A., et al. 2022, *AJ*, 164, 217 8
- Tomaney, A. B., & Crotts, A. P. S. 1996, *AJ*, 112, 2872 4
- Udalski, A., Szymański, M. K., & Szymański, G. 2015, *Acta Astronomica*, 65, 1 2
- Vehtari, A., Gelman, A., Simpson, D., Carpenter, B., & Bürkner, P.-C. 2021, *Bayesian Analysis*, 16, 667 17
- Wang, S., Wang, L., & Dong, S. 2025, *ApJS*, 276, 40 5
- Yan, S., & Zhu, W. 2022, *Research in Astronomy and Astrophysics*, 22, 025006 2
- Yang, H., Zang, W., Gould, A., et al. 2022, *MNRAS*, 516, 1894 4
- Yang, H., Yee, J. C., Hwang, K.-H., et al. 2024, *MNRAS*, 528, 11 4
- Yang, H., Yee, J. C., Zhang, J., et al. 2025, *AJ*, 169, 295 4
- Yee, J. C., Shvartzvald, Y., Gal-Yam, A., et al. 2012, *ApJ*, 755, 102 4
- Zang, W., Han, C., Kondo, I., et al. 2021, *Research in Astronomy and Astrophysics*, 21, 239 3

Zang, W., Jung, Y. K., Yee, J. C., et al. 2025, *Science*, 388, 400 2

Zhang, J., Zang, W., Ryu, Y.-H., et al. 2026a, *MNRAS*, 545, staf1893 6, 7, 15

Zhang, J., Zang, W., Udalski, A., et al. 2026b, arXiv e-prints, arXiv:2601.13276 7, 15

Zhang, K. 2023, *MNRAS*, 523, 1514 6

Zhu, W., & Dong, S. 2021, *ARA&A*, 59, 291 2

Zhu, W., Udalski, A., Novati, S. C., et al. 2017, *AJ*, 154, 210 13, 14